Available online at www.sciencedirect.com
ScienceDirect
Ultramicroscopy 108 (2007) 17–28
ultramicroscopy
www.elsevier.com/locate/ultramic

Depth sectioning in scanning transmission electron microscopy based on core-loss spectroscopy

A.J. D'Alfonso[a], S.D. Findlay[a], M.P. Oxley[b], S.J. Pennycook[b], K. van Benthem[b], L.J. Allen[a,*]

[a]School of Physics, University of Melbourne, Victoria 3010, Australia
[b]Materials Science and Technology Division, Oak Ridge National Laboratory, P.O. Box 2008, Oak Ridge, TN 37831, USA

Received 6 October 2006; received in revised form 7 February 2007; accepted 13 February 2007

Abstract

Recent and ongoing improvements in aberration correction have opened up the possibility of depth sectioning samples using the scanning transmission electron microscope in a fashion similar to the confocal scanning optical microscope. We explore questions of principle relating to image interpretability in the depth sectioning of samples using electron energy loss spectroscopy. We show that provided electron microscope probes are sufficiently fine and detector collection semi-angles are sufficiently large we can expect to locate dopant atoms inside a crystal. Furthermore, unlike high angle annular dark field imaging, electron energy loss spectroscopy can resolve dopants of smaller atomic mass than the supporting crystalline matrix.
© 2007 Elsevier B.V. All rights reserved.

PACS: 61.85.+p; 68.37.Lp; 82.80.Pv

Keywords: STEM; Depth sectioning; Nonlocality; Electron energy loss spectroscopy

1. Introduction

The ability to routinely obtain atomic resolution images of crystalline samples with the scanning transmission electron microscope (STEM) has opened up new avenues for materials research [1]. The properties of many materials, including semiconductors, catalysts and ceramics, have been observed to change with the addition of dopant atoms within the bulk [2–4]. The knowledge of impurity atom location will enable some material properties like electron mobility and catalyst stability to be estimated. Atomic resolution STEM imaging is beginning to offer the tantalising possibility to depth section samples and so extract 3D atomic locations [5–7].

The confocal scanning optical microscope (CSOM) is routinely used for 3D imaging at a resolution limit approximately equivalent to the wavelength of the optical photon used i.e. a few hundred nanometers. A CSOM constructs a 3D image by raster scanning a focussed light beam throughout the sample. To enable optical slicing or sectioning of the sample the CSOM produces images with a narrow depth of focus. The depth of focus observed in the image is determined by the size of a pinhole aperture placed just prior to the detector and the axial resolving power of the objective lens. Einspahr and Voyles [8] have reported optimum operating conditions for a confocal STEM, an electron microscope adaption of the CSOM. The confocal STEM differs from the conventional STEM with the addition of a post specimen collector lens. The inclusion of the lens creates a real-space image of the focussed probe at the detector. Two-dimensional confocal STEM imaging has been demonstrated by Frigo et al. [9] but not at atomic resolution. Here we explore whether with a conventional STEM one can attain lateral atomic resolution and nanometer depth resolution.

The development of aberration-correcting electron optics has increased the angular range of incident electrons that can be used to form a diffraction-limited probe, facilitating an increase in probe-defining aperture size and resulting in sub-Ångstrom probes [10,11]. Smaller probe

*Corresponding author. Tel.: +61 3 8344 7402; fax: +61 3 9347 4783.
E-mail address: lja@physics.unimelb.edu.au (L.J. Allen).

0304-3991/$ - see front matter © 2007 Elsevier B.V. All rights reserved.
doi:10.1016/j.ultramic.2007.02.026

size has increased the transverse resolution of the STEM while simultaneously producing a reduced depth of focus. Whilst the CSOM and conventional STEM detectors influence the image differently, it is proposed that STEM depth sectioning has similar experimental probe constraints to the CSOM; STEM depth sectioning demands the electron probe has a narrow depth of focus. The STEM probe and detector sizes ultimately determine the feasibility of 3D structure determination. The scheme proposed for depth sectioning is illustrated in Fig. 1. The narrow depth of focus in Fig. 1 corresponds to there being a significant proportion of the electron intensity located at the focal position.

In high angle annular dark field (HAADF) imaging, the contrast scales with the target's atomic mass approximately as Z^2. Supposing that the surrounding crystal is composed of atoms that are considerably lighter in mass than the dopant species, dopant detection should be possible. Voyles and co-workers [12,13] used probe channelling in HAADF simulations to show that it may be possible to resolve the depth of substitutional dopant (Bi and Sb) atoms, but this depends upon the surrounding bulk. Borisevich et al. [14] also presented simulations illustrating the identification of individual Bi atoms at differing depths within a Si crystal. Experimental results supporting the depth sectioning concept have been presented by several authors. Wang et al. [5] used defocus tuning to detect La atoms on the surface of doped γ-Al_2O_3 flakes, determining sample thickness with nanometer precision. Van Benthem et al. [7] reported the axial location of Hf atoms inside SiO_2 to nanometer precision. Borisevich et al. [6] constructed a 3D rendering of a (Pt,Au)/TiO_2 sample showing the distribution of metal nanoparticles from a through depth series of images. In all cases the dopant species were considerably heavier than the surrounding crystal species.

The relative mass differences between crystal and dopant species is an important condition of HAADF depth sectioning, but spectroscopic identification of dopant atoms is not subject to this condition. Electron energy loss spectroscopy (EELS) allows the identification of atomic species [15], replacing the HAADF dependence upon the target's atomic weight with that of the specific energy loss of a particular inner-shell ionization event. Scanning the probe through the sample enables the construction of a spectroscopic map of the sample. The feasibility of using EELS signals for depth sectioning will be discussed. The conclusions drawn illustrate that theoretical modelling of EELS is essential for experimental planning and interpretation.

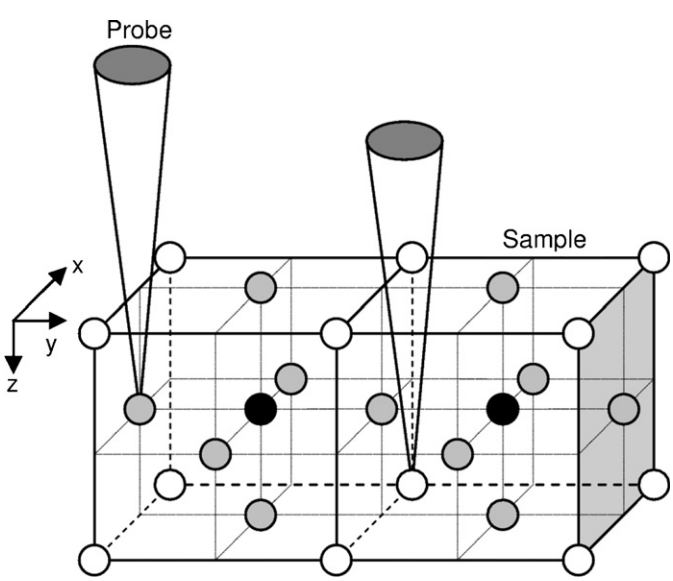

Fig. 1. The STEM depth sectioning scheme. Varying defocus Δf, in addition to the usual lateral scanning, enables the probe to be raster scanned throughout the sample in three dimensions (x, y, z).

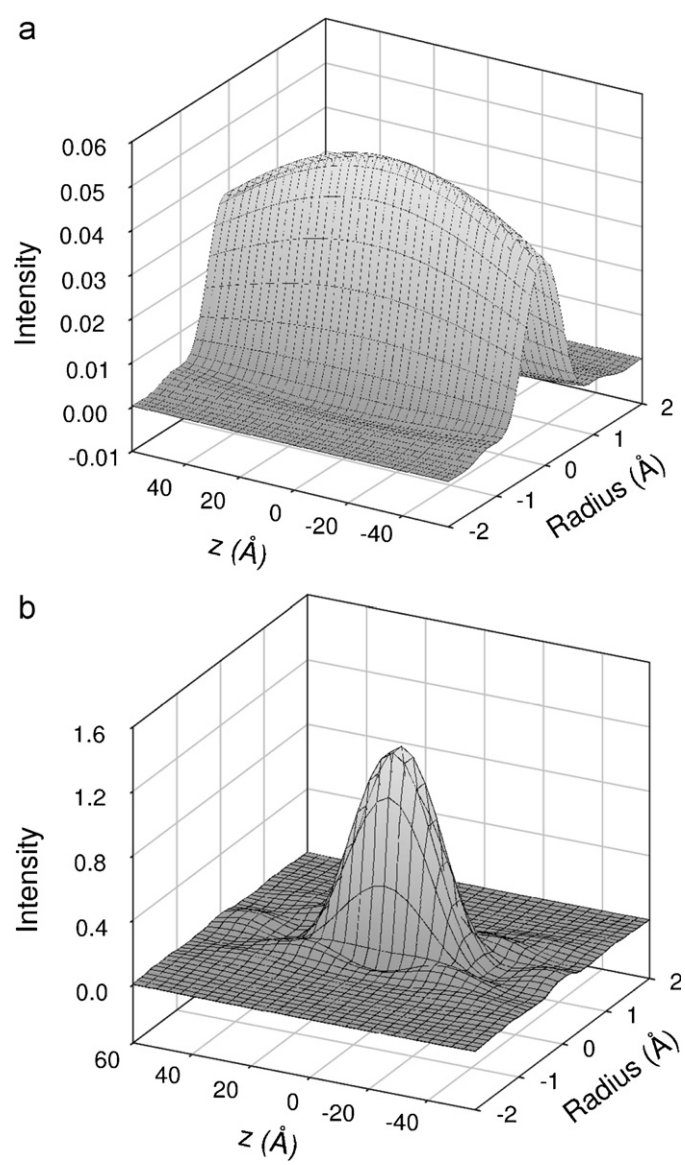

Fig. 2. Free space intensity profiles for a diffraction-limited 200 keV probe with probe forming apertures (a) $\alpha = 17$ mrad and (b) $\alpha = 37.5$ mrad.

2. The electron probe

A diffraction-limited electron probe may be described in free space as

$$\psi(\mathbf{R},\mathbf{r}_\perp,z) = \int O(q)\exp[-i\pi\lambda q^2(\Delta f + z)] \times \exp[2\pi i\mathbf{q}\cdot(\mathbf{r}_\perp - \mathbf{R})]\,\mathrm{d}\mathbf{q}, \quad (1)$$

where $\mathbf{q}$ is the transverse electron momentum of magnitude q, Δf is defocus (overfocus positive), λ denoting the relativistically corrected electron wavelength, $\mathbf{r}_\perp$ is a general position vector and $\mathbf{R}$ is the probe displacement, all parallel to the xy plane. The aperture pupil function $O(q)$ is a circular top hat function whose radius $q_{\max}$ limits the maximum transverse momentum contained within the probe. As the probe intensity distribution is axially symmetric, a cross section of the distribution suffices to describe the full 3D electron density profile. Fig. 2 illustrates how the electron intensity distribution changes as one increases the maximum allowed transverse momentum $q_{\max}$. The electron intensity in Fig. 2 is well localized on axis. The intensity distribution along the axis describes what we will refer to as the depth of focus and in both cases is fairly broad. As the probe forming aperture increases, going from Fig. 2(a) to Fig. 2(b), note how the depth of focus decreases. Evaluating the probe function in Eq. (1), for zero STEM probe displacement ($\mathbf{R} = \mathbf{0}$) and zero defocus ($\Delta f = 0$ Å), gives [16]

$$\psi(\mathbf{r}_\perp,z) = 2\pi\int_0^{q_{\max}} q\exp(-\pi i\lambda q^2 z)J_0(2\pi q r_\perp)\,\mathrm{d}q. \quad (2)$$

Evaluating the intensity profiles in the transverse and axial directions:

$$I(r_\perp) = |\psi(\mathbf{r}_\perp, z=0)|^2 = \left[\frac{q_{\max}J_1(2\pi q_{\max}r_\perp)}{r_\perp}\right]^2,$$

$$I(z) = |\psi(\mathbf{r}_\perp = \mathbf{0}, z)|^2 = \left[\pi q_{\max}^2\,\mathrm{sinc}\left(\frac{\pi\lambda q_{\max}^2 z}{2}\right)\right]^2. \quad (3)$$

It readily follows that the full width at half maximum (FWHM) values of the probe transverse spot size and depth of focus are:

$$r_{\mathrm{FWHM}} = \frac{0.5145}{q_{\max}} \approx \frac{0.5145\lambda}{\alpha},$$

$$z_{\mathrm{FWHM}} = \frac{1.772}{\lambda q_{\max}^2} \approx \frac{1.772\lambda}{\alpha^2}. \quad (4)$$

The implication of Eq. (4) for the free space probe is that the depth of focus (z_{FWHM}) decreases more rapidly than the transverse spot size (r_{FWHM}) for larger probe forming aperture semi-angles α. From Eq. (4) it is noted that currently available probe forming apertures can produce probes which have sub-Ångstrom transverse spot size [17] and depth of focus approaching 30 Å. In most materials the vertical unit cell sizes are typically of the order 5 Å and having a depth of focus of 30 Å may make ultra high resolution depth sectioning impossible. It must be appreciated, however, that reliable qualitative depth interpretation is not entirely dependent upon probe depth resolution. There is a clear distinction between the precision to which one can determine dopant depth and the depth resolution of a probe. Accurate theoretical simulations of experimental images can enable precise structure determination from probes having relatively poor depth resolution [7].

3. Calculation of the inelastic cross section

The depth sectioning approach depicted in Fig. 1 requires the image signal to be dominated by the contribution from the 3D position of the beam waist. This scenario is described by the conventional local potential

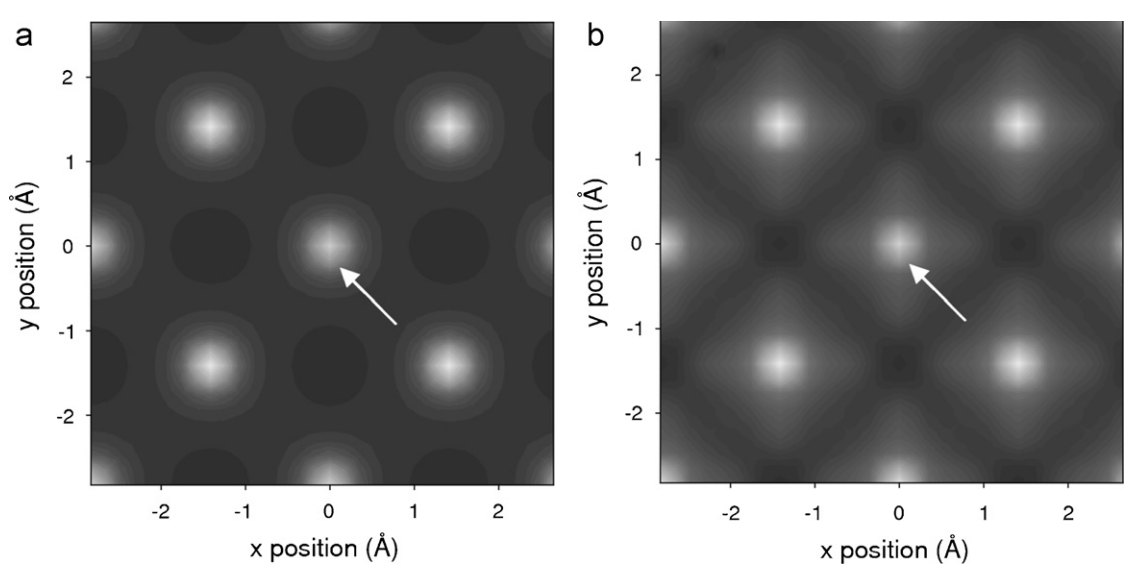

Fig. 3. HAADF reference image of a ⟨1 0 0⟩ zone axis $Al_xGa_{1-x}As$ crystal 120 Å thick with a probe forming aperture of $\alpha = 37.5$ mrad. The annular detector spans 60–160 mrad. The 200 keV probe had (a) $\Delta f = 0$ Å and (b) $\Delta f = -60$ Å. The substitutional Al dopant is located on a Ga column at $(x, y, z) = (0, 0, 62)$ Å indicated by the white arrows.

imaging model, thus assuming an electron of mass m incident onto a crystal surface of area A in the xy plane allows the cross section to be calculated as [18,19]:

$$\sigma(\mathbf{R}) = \frac{4\pi}{hv}\int_0^t \int_A |\psi(\mathbf{R}, \mathbf{r}_\perp, z)|^2 V_{\text{inel}}(\mathbf{r}_\perp, z)\, \mathrm{d}\mathbf{r}_\perp\, \mathrm{d}z. \quad (5)$$

Here the local inelastic potential is V_{inel}, h is Planck's constant, $v = hk_0/m$ is the incident electron velocity, $\lambda_0 = 1/k_0$ is the relativistic electron wavelength and t is the crystal thickness. Eq. (5) is adequate for simulating HAADF images and using a projected potential approximation allows V_{inel} to be modified for successive slices to fit within a multislice framework. This framework facilitates discussion about the contributions to images from particular slices, specifically those contributions from slices containing impurities as we can modify the slice potential to accommodate the impurity. The effective local crystal scattering potential seen by

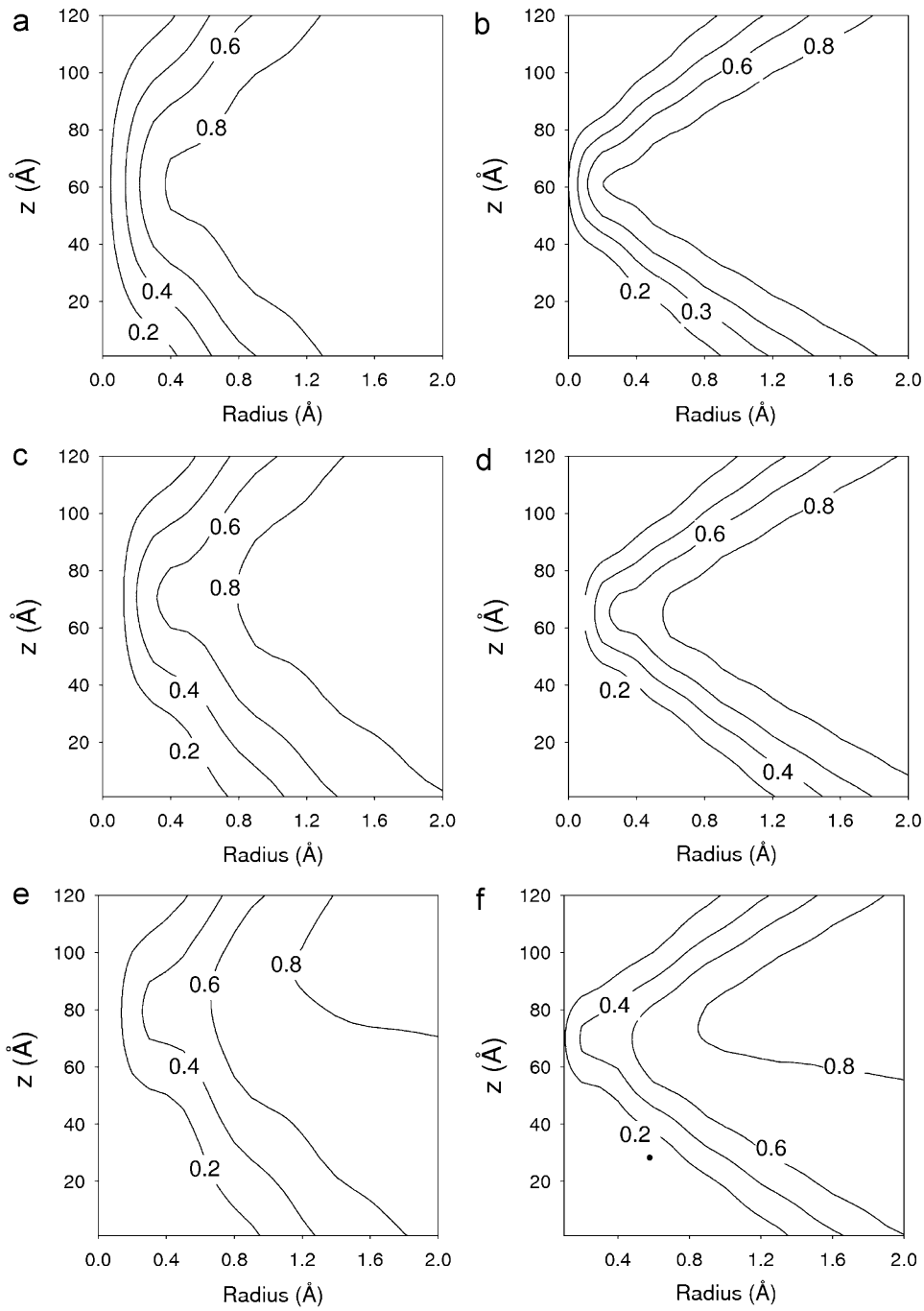

Fig. 4. Proportion of the electron probe intensity as a function of radial distance from the column for a 200 keV probe with defocus $\Delta f = -60$ Å. The free space (non-interacting) scenario is shown with probe forming apertures (a) $\alpha = 25$ mrad and (b) $\alpha = 37.5$ mrad. Situating the probe above a Si column in Si crystal oriented along $\langle 1\,0\,0 \rangle$ is shown with probe forming apertures (c) $\alpha = 25$ mrad and (d) $\alpha = 37.5$ mrad. Finally, the probe intensity in a GaAs crystal oriented along $\langle 1\,0\,0 \rangle$ when the probe is placed above the Ga column is presented with probe forming apertures (e) $\alpha = 25$ mrad and (f) $\alpha = 37.5$ mrad.

the probe is [21]

$$V_{\text{inel}}(\mathbf{r}_\perp) = \frac{\pi m}{h^2 t}\sum_{n\neq 0}\frac{1}{k_n}\sum_{\alpha}|H_{\alpha,n0}(\mathbf{r}_\perp)|^2, \tag{6}$$

where $H_{\alpha,n0}$ is the projected transition matrix element of the interaction Hamiltonian going from state 0 to state n for atom α in the sample and k_n is the magnitude of the scattered electron wave vector.

It would be convenient but not necessarily realistic to describe the inelastic processes in which electrons get scattered to the detector as being local. However, spectroscopic techniques may require a full nonlocal treatment [20], Eq. (5) being an inadequate description for the spectroscopic image. In the nonlocal model the scattering cross section is given by

$$\sigma(\mathbf{R}) = \frac{2\pi}{hv}\int_0^t\int_A\int_A \psi^*(\mathbf{R},\mathbf{r}_\perp,z)W_{\text{inel}}(\mathbf{r}_\perp,\mathbf{r}'_\perp) \times \psi(\mathbf{R},\mathbf{r}'_\perp,z)\,\mathrm{d}\mathbf{r}_\perp\,\mathrm{d}\mathbf{r}'_\perp\,\mathrm{d}z, \tag{7}$$

where, making the flat Ewald sphere approximation, the effective projected nonlocal potential is [21]

$$W_{\text{inel}}(\mathbf{r}_\perp,\mathbf{r}'_\perp) \approx \frac{2\pi m}{h^2 t}\sum_{n\neq 0}\sum_{\alpha}\frac{1}{k_n}H^*_{\alpha,n0}(\mathbf{r}_\perp)H_{\alpha,n0}(\mathbf{r}'_\perp) \times \int \exp[2\pi i\mathbf{K}'_\perp\cdot(\mathbf{r}_\perp-\mathbf{r}'_\perp)]\,\mathrm{d}\mathbf{K}'_\perp, \tag{8}$$

with K' denoting the magnitude of the scattered electron wave vector. Fourier expanding Eq. (8), the resulting Fourier coefficients may be identified as the inelastic scattering coefficients:

$$W_{\text{inel}}(\mathbf{r}_\perp,\mathbf{r}'_\perp) = \frac{hv}{2\pi A}\sum_{\mathbf{g},\mathbf{h}}\mu_{\mathbf{h},\mathbf{g}}\mathrm{e}^{2\pi i\mathbf{h}\cdot\mathbf{r}_\perp}\mathrm{e}^{-2\pi i\mathbf{g}\cdot\mathbf{r}'_\perp}, \tag{9}$$

with general Fourier transform space vectors $\mathbf{g}$ and $\mathbf{h}$ as defined by the supercell used in computation. The potential is deemed nonlocal due to the dependence on two independent spatial variables.

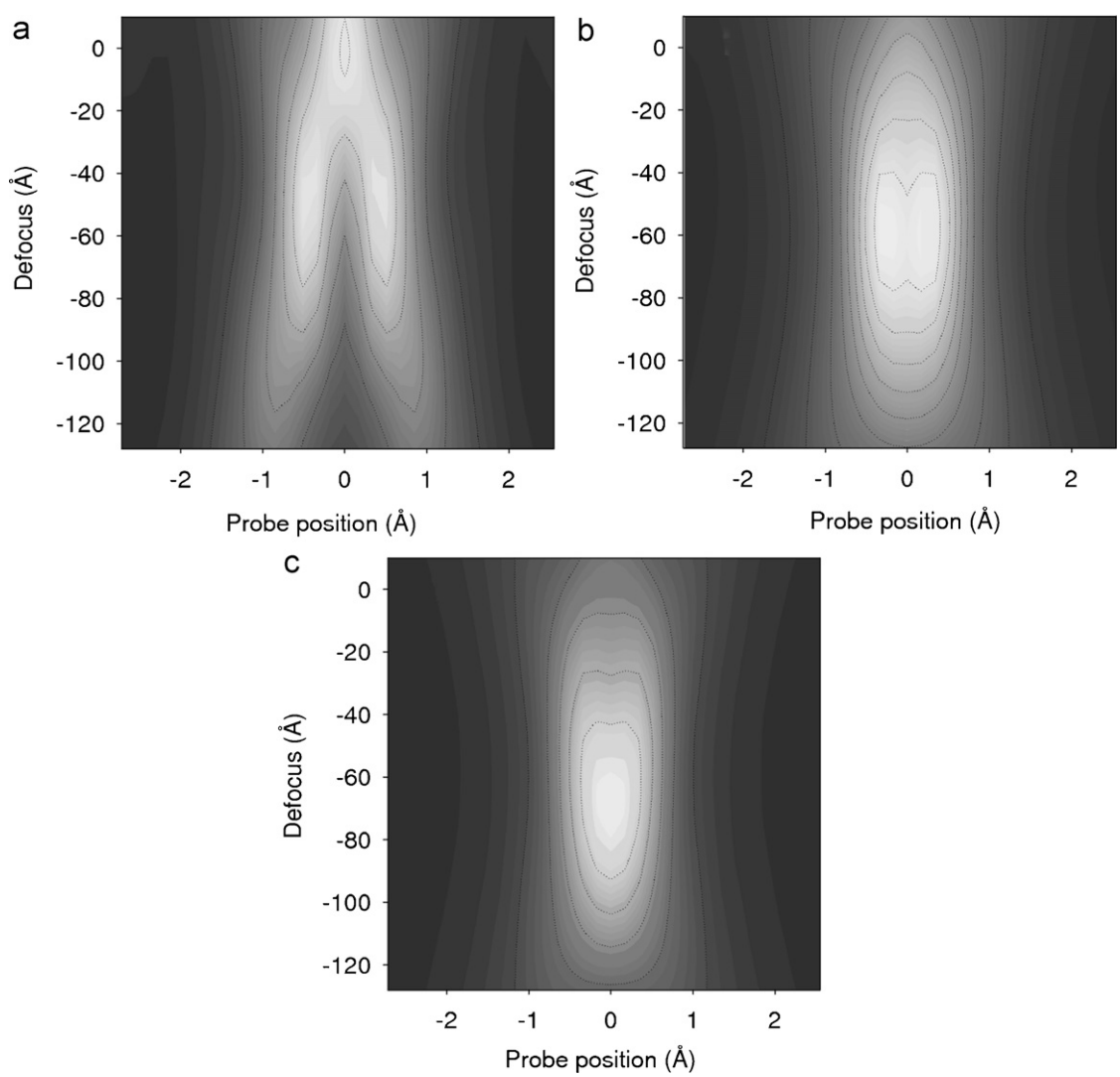

Fig. 5. Sb M-shell EELS probe line scan simulations along ⟨0 0 1⟩. The Sb atom is embedded 65 Å deep on a Si column at $x = 0$ Å in a Si crystal oriented along the ⟨1 0 0⟩ zone axis. The consequence of increasing EELS detector collection semi-angles, (a) $\beta = 10$ mrad, (b) $\beta = 30$ mrad and (c) $\beta = 50$ mrad, is shown. The 200 keV probe had a $\alpha = 25$ mrad probe forming aperture.

For thermal scattering in the Einstein model the inelastic scattering coefficients $\mu_{\mathbf{h},\mathbf{g}}$ are [22]

$$\mu_{\mathbf{h},\mathbf{g}} = \frac{1}{V_c}\sum_n \exp[2\pi i(\mathbf{g}-\mathbf{h})\cdot\boldsymbol{\tau}_n]\int f_n(\mathbf{Q}+\mathbf{g})f_n^*(\mathbf{Q}+\mathbf{h}) \times\{\exp[M_n(\mathbf{g}-\mathbf{h})]-\exp[M_n(\mathbf{Q}+\mathbf{g}) - M_n(\mathbf{Q}+\mathbf{h})]\}\,\mathrm{d}\Omega_{K'}, \quad (10)$$

where $h\mathbf{Q} = h(\mathbf{K}-\mathbf{K}')$ is the momentum transfer from the incident electron to the crystal. $M_n(\mathbf{q}) = 2\pi^2\langle u_n^2\rangle q^2$ is the Debye–Waller factor, where the projected mean square thermal vibration amplitude $\langle u_n^2\rangle$ describes the smearing of the potential due to the thermal motion of atoms. The sum occurs over all atoms of scattering factor f_n located at the position $\boldsymbol{\tau}_n$ in a unit cell of volume V_c. The HAADF image will contain contributions from all regions where the electron intensity is non-zero. The HAADF integration through t in Eq. (5) limits the thickness of the sample one can use for depth sectioning. The thickness integration implies that the contribution of one impurity will be insignificant compared with the column total for sufficiently thick samples: any extra contribution from the impurity is masked by the column total. Supposing the sample is sufficiently thin, the effective scattering potential of the impurity atom will only generate significant contributions over those of the column if the atomic mass of the impurity is significantly larger than the column species.

However, provided the spectral characteristics of the impurity atom do not overlap with those of the supporting structure, spectroscopic techniques such as EELS can produce signals deriving from the impurity alone, unmasked by the supporting structure. The EELS inelastic scattering coefficients are [23]

$$\mu_{\mathbf{h},\mathbf{g}} = \frac{1}{2\pi K V_c}\sum_n \exp[-M_{\beta_n}(\mathbf{g}-\mathbf{h})] \times\exp[2\pi(\mathbf{g}-\mathbf{h})\cdot\boldsymbol{\tau}_{\beta_n}]f(\mathbf{h},\mathbf{g}). \quad (11)$$

The sum in Eq. (11) is now restricted to specific atomic species β at position $\boldsymbol{\tau}_{\beta_n}$ within the unit cell. The Debye–Waller factor accounts for the thermal motion of the atoms. The scattering factor $f(\mathbf{h},\mathbf{g})$ is given by

$$f(\mathbf{h},\mathbf{g}) = \frac{1}{2\pi^3 a_0^2}\int\int K'\frac{F^*(\mathbf{Q}+\mathbf{h},\boldsymbol{\kappa})F(\mathbf{Q}+\mathbf{g},\boldsymbol{\kappa})}{|\mathbf{Q}+\mathbf{h}|^2|\mathbf{Q}+\mathbf{g}|^2}\,\mathrm{d}\boldsymbol{\kappa}\,\mathrm{d}\Omega_{K'}, \quad (12)$$

where a_0 is the relativistically corrected Bohr radius. The transition matrix elements are

$$F(\mathbf{Q}+\mathbf{g},\boldsymbol{\kappa}) = \int u_f(\boldsymbol{\kappa},\mathbf{r}')\exp[2\pi(\mathbf{Q}+\mathbf{g})\cdot\mathbf{r}']u_i(\mathbf{r}')\,\mathrm{d}\mathbf{r}'. \quad (13)$$

The transition matrix element is for a specific suborbital occupied by the target electron in the atomic species. We denote the normalized continuum and bound state wave functions of the target electron as $u_f(\boldsymbol{\kappa},\mathbf{r}')$ and $u_i(\mathbf{r}')$, respectively. Calculation of the target electron wave functions can be made using Hartree–Fock based wave functions [24]. The detector energy window ΔE limits the range of the ejected electron's wave vector $\boldsymbol{\kappa}$ for a given momentum transfer. The $\mathrm{d}\Omega_{K'} = \sin\theta\,\mathrm{d}\theta\,\mathrm{d}\phi$ integration is restricted to the collection semi-angle of the detector. The inelastic scattering coefficients contain the mixed dynamical form factors (MDFFs) necessary for incoherent scattering. For further discussion of the MDFFs and their physical significance see Schattschneider et al. [25,26].

4. Results

Consider two test scenarios: Al in a GaAs crystal and Sb in a Si crystal. As a member of the group III–V semiconductor family, the $Al_xGa_{1-x}As$ heterostructure has received much scientific attention [27] making it an excellent candidate for exploratory study. HAADF is unable to resolve a single substitutional Al dopant as it has a significantly smaller atomic mass than the supporting GaAs crystal. The Al K-shell ionization edge lies at 1560 eV [15] and is an excellent candidate to demonstrate the principles of EELS depth sectioning. Simulations for

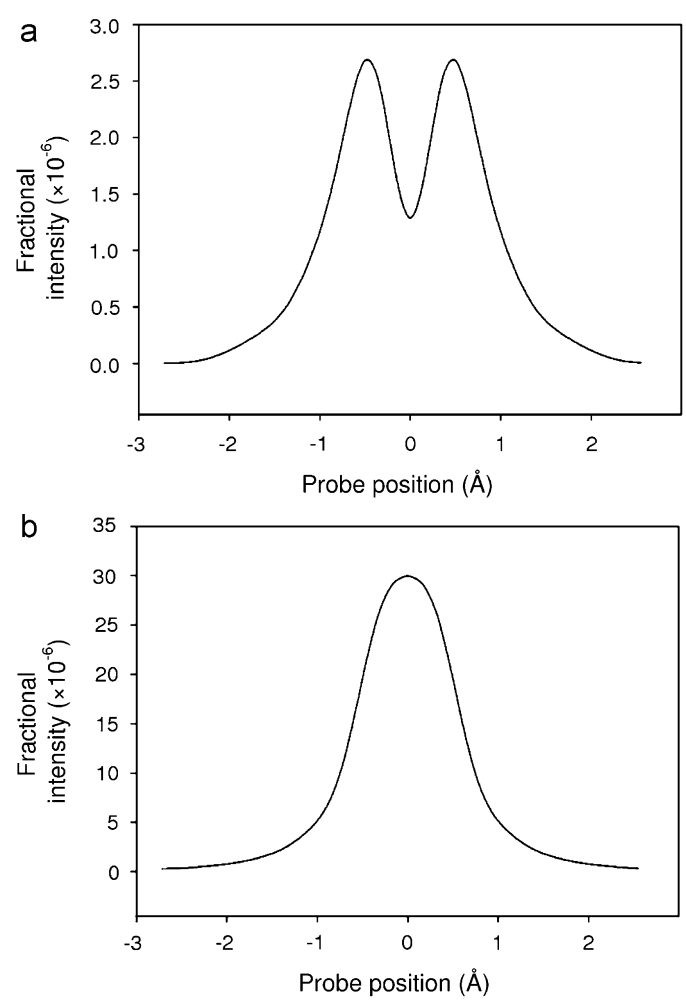

Fig. 6. Sb M-shell EELS probe line scans for Sb in Si ⟨1 0 0⟩ crystal. Extracts from Fig. 5 with $\Delta f = -70$ Å using (a) $\beta = 10$ mrad and (b) $\beta = 50$ mrad electron collection semi-angles.

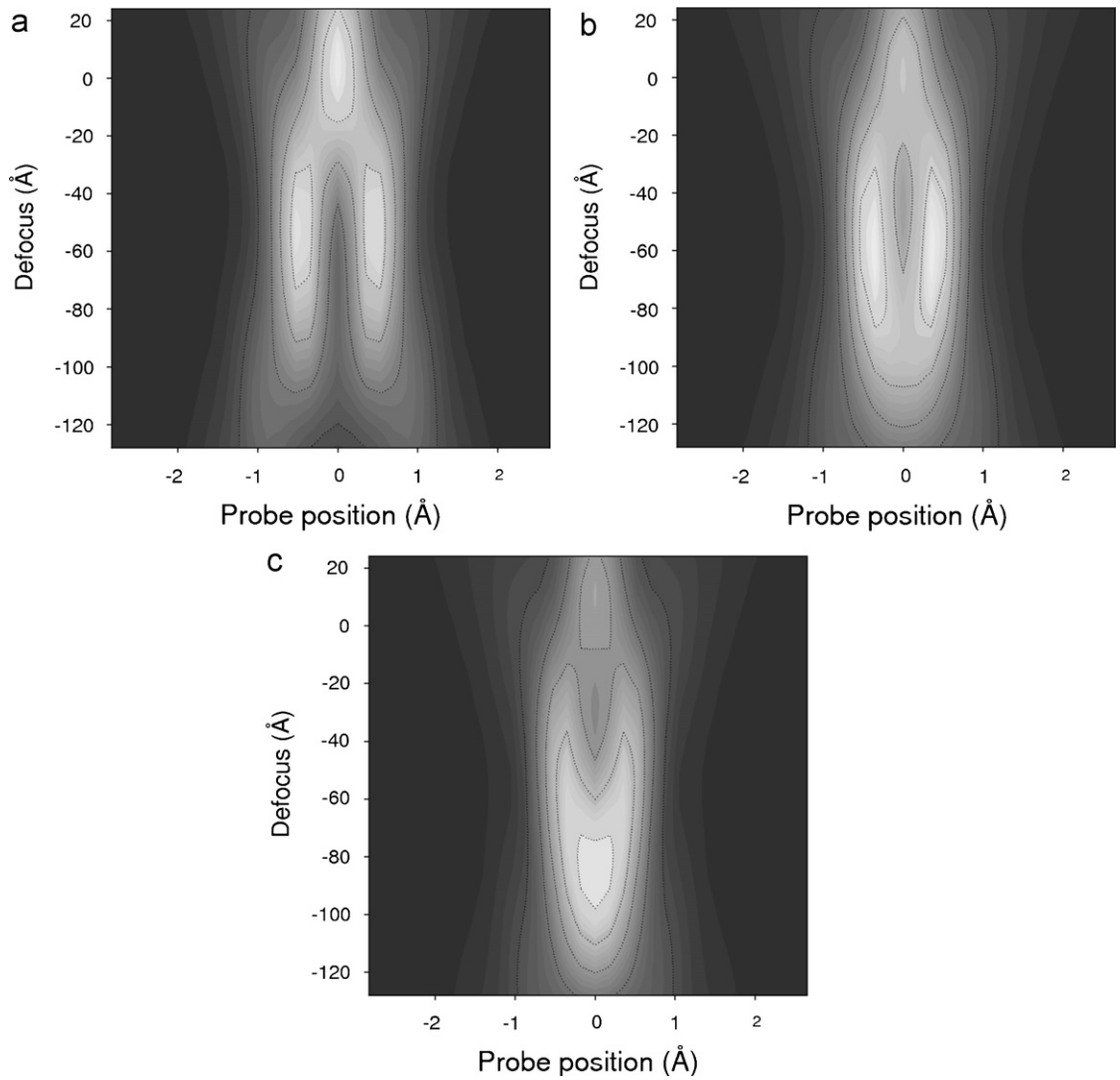

Fig. 7. Al K-shell EELS probe line scan simulations along ⟨0 0 1⟩. The Al atom is embedded 62 Å deep on a Ga column at $x = 0$ Å in a GaAs crystal oriented along the ⟨1 0 0⟩ zone axis. The consequence of increasing EELS detector collection semi-angles, (a) $\beta = 10$ mrad, (b) $\beta = 30$ mrad and (c) $\beta = 50$ mrad, is shown. Simulations used a 200 keV probe with probe forming aperture $\alpha = 25$ mrad.

the L-shell, which is experimentally more accessible, have the same general features but are more adversely affected by the nonlocality of the interaction and so are not shown here. The simulations presented involved substituting an Al atom for a Ga atom at various depths into a Ga column. Whilst HAADF Sb in Si crystal simulations have been reported [12] we present a set of complementary Sb EELS results showing the spectroscopic identification of the dopant Sb within the Si bulk. The Sb edge considered was the $M_{4,5}$ edge at 528 eV [15]. The Sb in Si crystal simulations also involved artificially replacing a single Si atom with a Sb dopant on column. The GaAs and Si crystals were both aligned along the ⟨1 0 0⟩ zone axis. The simulations assume a 200 keV diffraction-limited probe with user-variable defocus. The EELS signal was integrated up over a 40 eV energy window above ionization threshold. (This energy window may be too small to collect much signal in practice from the delayed Sb $M_{4,5}$ edge but within our simulations this does not affect the form of our results, only their scale.) The HAADF images, using a local approximation ($\mu_{\mathbf{h-g},0}$), and EELS results, using the nonlocal potential in Eq. (8), were calculated via multislice techniques as described in Ref. [19].

4.1. Reference HAADF image

To perform STEM EELS depth sectioning the procedure requires the simultaneous recording of both HAADF images and EELS spectra. The HAADF image is used as a structural reference to allow alignment of the EELS spectra to the columns. To enable accurate alignment the HAADF image must contain sufficient contrast. It has been reported that the optimal HAADF probe forming aperture semi-angle α which results in the greatest image contrast may not necessarily be the largest available [28], rather it is the probe whose width is comparable to the

columns 1s-like state which is optimal. Rephrased, the finest probe may not produce the most interpretable images of the whole crystal. Nevertheless it is found that opening the probe forming aperture to $\alpha = 37.5$ mrad, beyond the optimum coupling value for the experiment, produces a simulated HAADF reference image that is qualitatively interpretable for a range of differing defocus values Δf (see Fig. 3).

4.2. Role of the crystal in altering the probe properties

Large probe forming aperture semi-angles result in finer probes that should interact weakly with the surrounding crystal. This is pertinent to depth sectioning as the scheme relies upon a narrow beam waist whose location can be adjusted by varying Δf. Wolf [29] produced contour plots detailing the fractional intensity present on circular discs for perfectly spherical waves emanating from a circular aperture. Here we present the analogous STEM case. The radial integration of the electron probe intensity surrounding a column at different depths within the crystal shows the evolution of the probe and the effect of the crystal on the electron intensity distribution. Electron probe intensity calculations for free space and the two test cases are presented in Fig. 4. The free space situation represents the ideal case where the probe does not interact with its surroundings. The narrow beam waist is illustrated by the localization of electron intensity at $z = 60$ Å in Figs. 4(a) and (b). The Si crystal electron intensity plots shown in Figs. 4(c) and (d) are considerably more symmetrical and contain a sharper beam waist than those of the contrasting GaAs crystal, Figs. 4(e) and (f). The sharper beam waist is indicated by the tighter cluster of contour lines in the region $z \approx 60$ Å. For heavier crystals the cluster not only spreads but also shifts the location of the waist along the column away from the set probe defocus. The shifting of

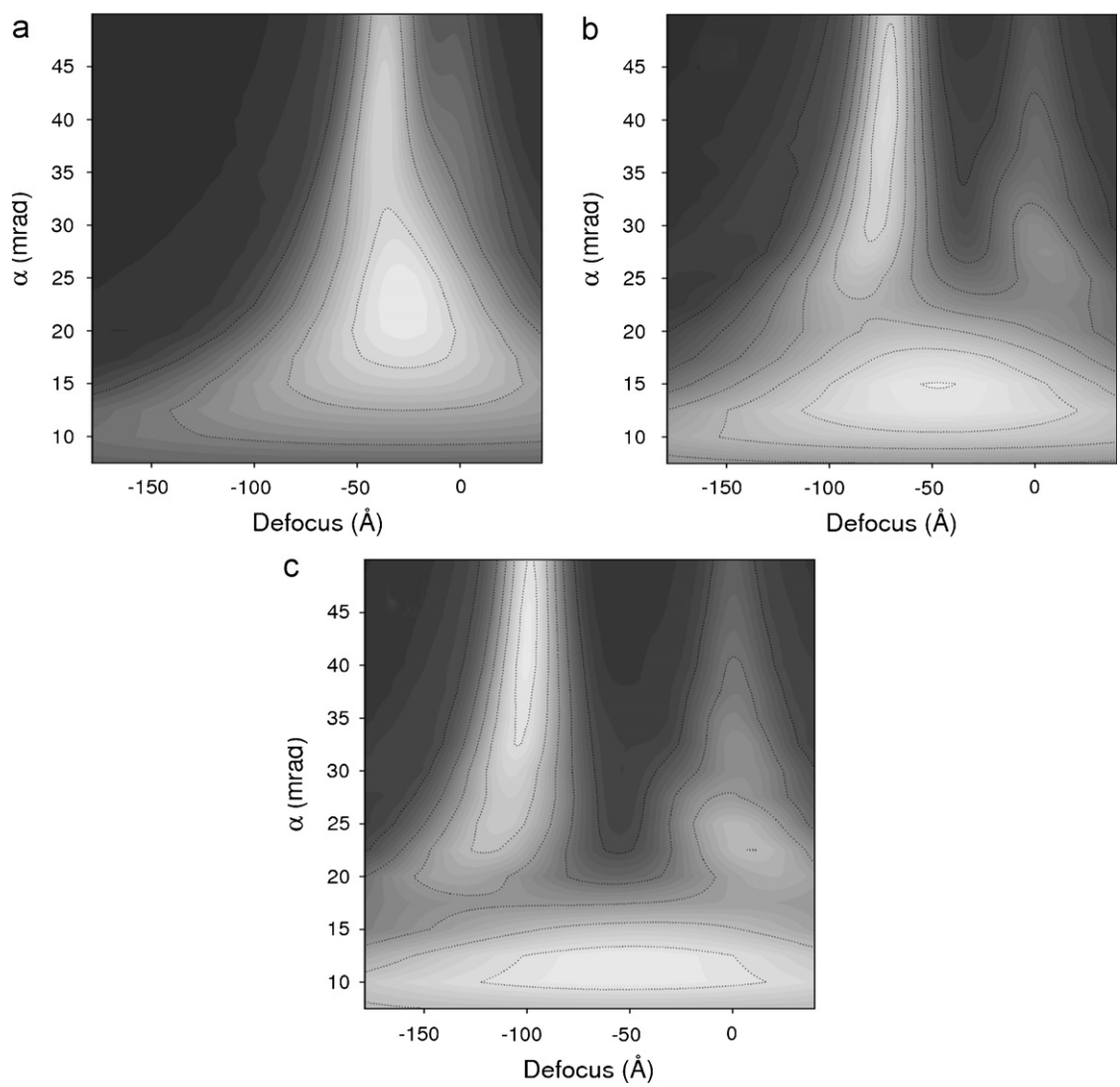

Fig. 8. Plots for various Al dopant depths, (a) 28 Å, (b) 62 Å and (c) 90 Å, relating the increase in aperture semi-angle α to the EELS intensity recorded. The GaAs crystal is oriented along the $\langle 1\,0\,0 \rangle$ zone axis. The 200 keV probe is located directly above the Ga column containing a single Al dopant atom. The detector collection semi-angle is $\beta = 50$ mrad. The grey intensity scales are independent to emphasise the local maxima occurring at $\Delta f \approx 0$ Å.

the beam waist toward the incident surface shows the influence of the crystal and specifically the atomic focussing of the probe. The narrow beam waist reflecting the desired operating regime presented in Fig. 1 can only be achieved with large probe forming apertures.

4.3. Role of the detector in localizing the image in the transverse direction

The nonlocal cross-section expression in Eq. (7) has the implicit assumption that the degree of interference of the inelastic wave originating at different points is determined by the form of the detector [30]. The details of the detector geometry are included implicitly in the potential via the integration over the scattered electron wave vector K' in Eq. (8). In the limit that the range of this integral tends to infinity the integration collapses to a delta function and the only non-zero elements in $W_{\text{inel}}(\mathbf{r}_\perp, \mathbf{r}'_\perp)$ occur along the diagonal. (This limit is not formally reached, but can be achieved in practice with suitably large collector apertures. What constitutes "sufficiently large" is discussed in Ref. [21].) This reduces the nonlocal expression Eq. (7) to the local expression Eq. (5) where there are no longer phasing effects. Supposing that the aberrations present in the electron collector optics can be corrected, having the two detector STEM geometry implies the EELS detector is limited to the collection semi-angle of the inner HAADF detector radius. Present collection semi-angles are much smaller than this so careful consideration of the extent to which a local interpretation for small collection semi-angles can be made must be undertaken.

Fig. 5 shows the effect of varying the electron detector collection semi-angle β on the image line scans along the x-axis $\langle 0\,0\,1 \rangle$. Within Fig. 5 the dopant Sb was placed on a Si column at $x = 0$ Å and a depth 65 Å. The negative defocus corresponds to the beam waist being located inside the crystal. In the z-direction, increasing the detector collection semi-angle serves to shift the maximum intensity recorded from the surface ($\Delta f = 0$ Å) of the crystal to the region inside the crystal near the dopant site ($\Delta f \approx -70$ Å). The appearance of volcano-like behaviour in the image when the defocus approximately equals the dopant depth is shown explicitly in Fig. 6(a) and is removed with the inclusion of larger collection semi-angles β, Fig. 6(b). Volcano behaviour for the given probe and collector parameters is also observed in isolated single atom cases. Volcano formation is discussed further by Kohl and Rose [31]. It would be convenient to define a pseudo-FWHM for depth response where one relates the recorded intensity as a function of probe defocus, similar to spatial resolution plots produced by Cosgriff et al. [32]. However, when $\alpha = 25$ mrad the emergence of double peaks and volcanoes complicates the interpretation of conventional z-direction FWHM values.

In Fig. 7, the Al dopant was placed on a Ga column at $x = 0$ Å and a depth of 62 Å. The image β dependence is explicitly shown in Fig. 7. Qualitative interpretation of the image when using a detector collection semi-angle $\beta = 10$ mrad suggests that the dopant is located on the surface of the crystal which is clearly an incorrect interpretation. The larger detector collection semi-angle $\beta = 30$ mrad has a smeared peak intensity that encompasses the entire defocus range. Finally, when the detector collection semi-angle $\beta = 50$ mrad the majority of the signal intensity is localised at $|\Delta f|$ approximately equal to the dopant depth. The peak intensity corresponding to dopant depth in Fig. 7(c) shows the over-focusing effect of the column. The peak intensity occurs for probes focused further into the crystal than the depth at which the dopant is located.

4.4. Role of the probe aperture size on the signal intensity at the dopant site

It has been shown that larger detector collection semi-angles result in more qualitatively interpretable images in the transverse and axial directions. Using a large detector with $\beta = 50$ mrad, the degree of precision to which one can establish the depth of a dopant with increasing probe aperture α is presented in Fig. 8. The simulations involved holding the probe position directly above the column and varying defocus.

Fig. 8 suggests a minimum probe forming aperture of $\alpha = 35$ mrad is required for the $Al_xGa_{1-x}As$ structure for an EELS detector subtending $\beta = 50$ mrad. Note the false peak clearly evident in Fig. 8(c) at $\Delta f = 0$ Å when the probe forming aperture is less than $\alpha = 25$ mrad. The false peak is comparable to the true peak ($\Delta f \approx -110$ Å) in magnitude, implying the possibility of falsely assuming that two dopants are present in the column. The origins of the false peak can be explained with examination of Fig. 9

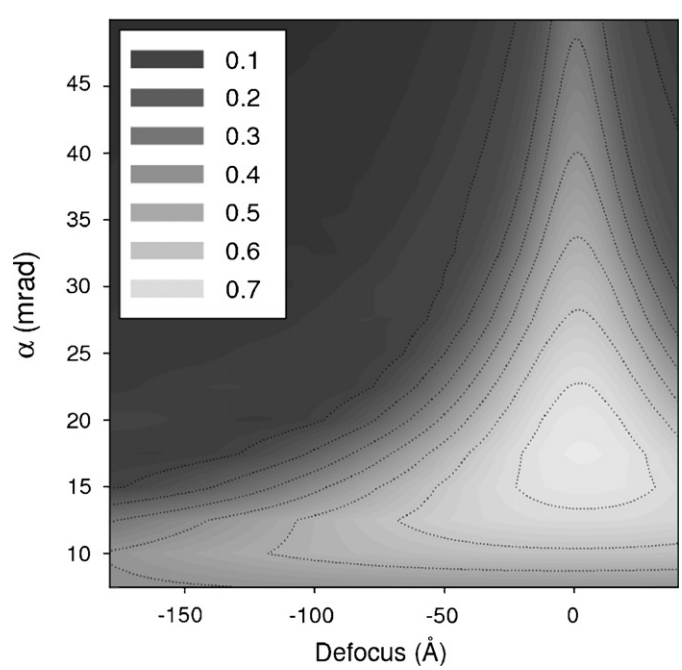

Fig. 9. The fraction of the 200 keV probe that is coupled to the Ga column 1s-like states for varying probe defocus and aperture sizes α.

which shows the fraction of the probe which couples to the 1s-like column states for the probe positioned above the Ga column (calculated following Ref. [33]). The maximum coupling of the probe to these states is achieved for a probe positioned on the surface when the width of the probe is commensurate with the width of the column 1s-like state. When the probe is focussed onto the surface and couples to the column 1s-like state, the subsequent electron channelling along the column generates ionization events at the dopant depth. This registers significant counts onto the detector for a defocus which does not correlate to the dopant depth.

Provided that the imaging system can produce sufficiently fine probes, Fig. 10 shows the results depth sectioning could provide for increasing collector sizes. When the probe forming aperture is large ($\alpha = 37.5$ mrad) and the collection semi-angle ($\beta = 10$ mrad) small the relative probe and detector sizes couple with a strongly absorbing Ga column to increase the effect of volcanoes (see Fig. 10(a)). Reversing the relative size difference and making the detector collection semi-angle $\beta = 50$ mrad (i.e. $\beta \geqslant \alpha$) returns results agreeing with a local model and suggests that qualitative dopant depth interpretation will be achievable (see Fig. 10(c)). Such geometries are currently not obtainable experimentally but may become achievable with next generation STEM equipment by using post specimen electron optical lenses.

4.5. Multiple impurities on column

We have seen that, for an isolated impurity, a number of factors affect the interpretation of depth sectioning based on EELS. For too small a probe forming aperture, there is strong coupling of the 1s-like state to the atomic column, resulting in a large artificial peak in the integrated EELS intensity when the probe is focused near the specimen's entrance surface. Fig. 8 demonstrates that there can be a significant 1s contribution even for impurities located at

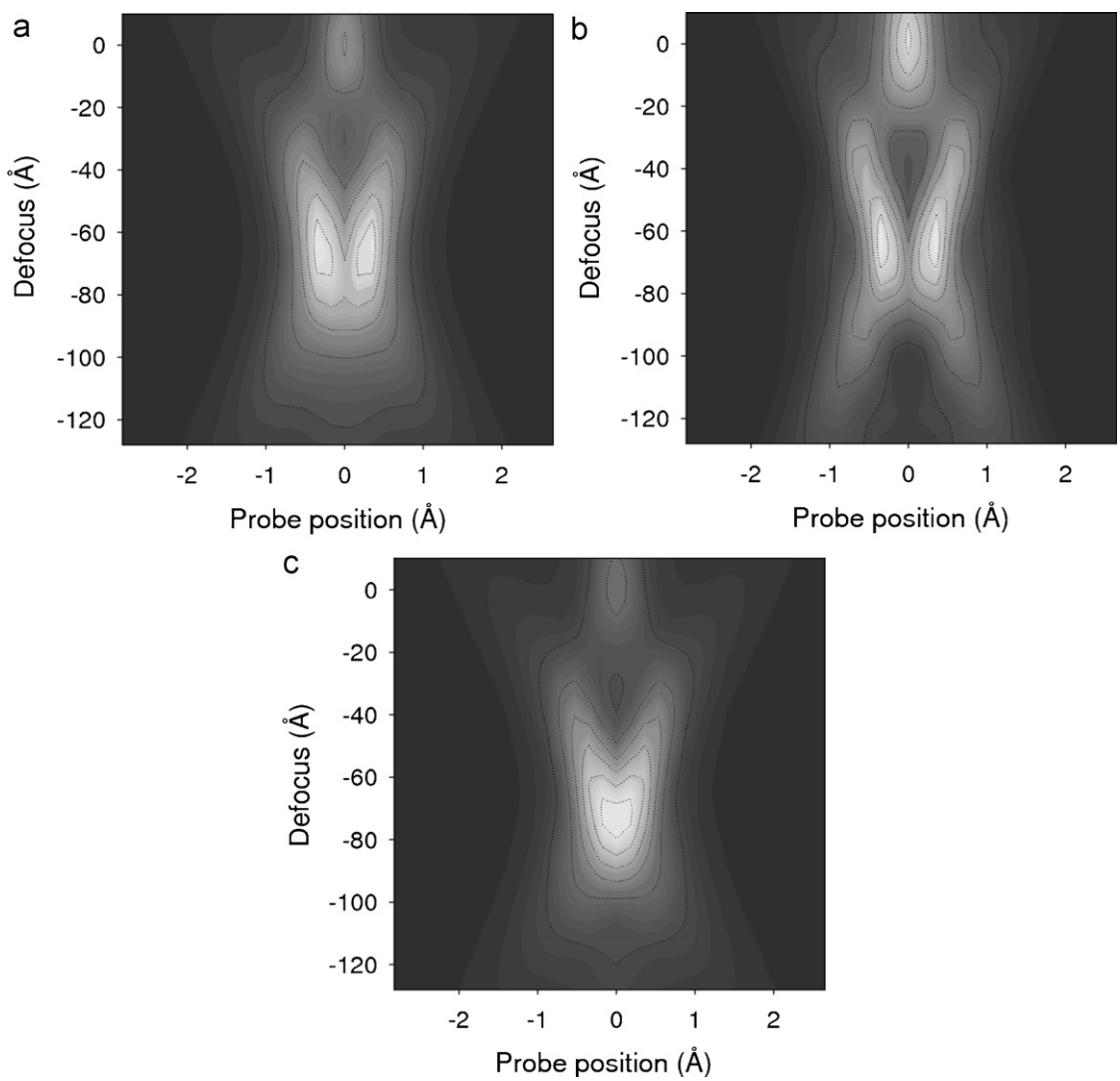

Fig. 10. Al K-shell EELS probe line scan simulations along ⟨0 0 1⟩. The Al atom is embedded on a Ga column 62 Å deep at $x = 0$ Å in a GaAs crystal oriented along the ⟨1 0 0⟩ zone axis. The consequence of increasing EELS detector collection semi-angles, (a) $\beta = 10$ mrad, (b) $\beta = 30$ mrad and (c) $\beta = 50$ mrad, is shown. Simulations used a 200 keV probe with probe forming aperture $\alpha = 37.5$ mrad.

significant depths. In addition the overfocussing of the electron probe due to the atomic column results in a shifting of the observed maximum signal away from the depth of the impurity. Given the difficulties in interpreting a focal series for a single impurity, what can be determined if more than one impurity is present?

In Fig. 11, we consider the case of two Al impurity atoms located in a Ga column in ⟨1 0 0⟩ zone axis oriented GaAs. These substitutional impurities are located at depths of 62 and 130 Å. The variation in intensity is shown as a function of defocus for probe forming apertures of 25 and 37.5 mrad in Figs. 11(a) and (b), respectively. For $\alpha = 25$ mrad we see a large contribution to the intensity from 1s coupling for the probe focused near the entrance surface. For the remainder of the focal range there is a smeared out peak centred between the dopants. This intensity distribution can be understood by examining Fig. 11(c) which shows the intensity on the Ga column as a function of defocus as well as the contributions from each dopant individually, which may be added to produce the total signal. Both impurities result in a strong signal due to 1s coupling for the probe focus near the surface adding to produce the maximum signal. The impurity at 62 Å produces a peak around a defocus of −80 Å which is significantly larger than its zero defocus contribution. The impurity at 130 Å, however, produces a peak at a defocus value of −160 Å with less than half this intensity. Because of the large depth of field there is significant overlap of these peaks and the individual impurities are not resolved. For the smaller probe used in Fig. 11(b) there are three clearly resolved peaks in intensity as a function of defocus. As seen in Fig. 11(d), the first is again due to the addition of the coupled 1s-like states from each impurity. Both impurities produce delayed intensity peaks with magnitudes greater than the 1s-like states and the decreased depth of field means that the individual peaks are clearly resolved.

5. Conclusion

It has been shown that geometric depth sectioning within the STEM using EELS signals is possible. Provided that aberration correctors continue to allow increases in probe convergence angles, depth sectioning will be possible on the nanometer scale due to a further reduced depth of focus. Probe coupling to the 1s-like state of the atomic column is a limiting concern which was demonstrated to place strict requirements on STEM probes. The nonlocal nature of the

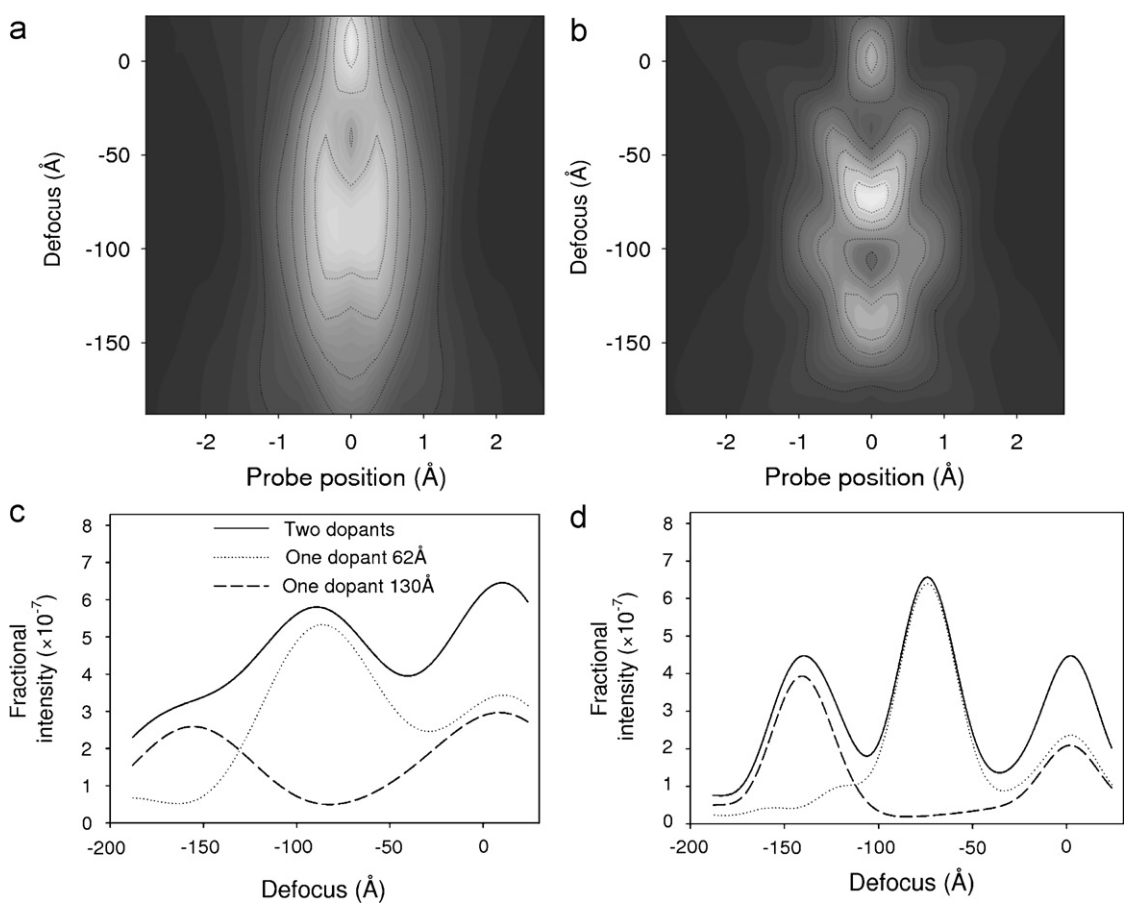

Fig. 11. Simulated Al K-shell EELS line scans as a function of defocus formed by a 200 keV probe with (a) $\alpha = 25$ mrad and (b) $\alpha = 37.5$ mrad, for Al impurities in ⟨1 0 0⟩ zone axis oriented GaAs. The substitutional Al impurities are located in the Ga column positioned at $x = 0$ Å at depths of 62 and 130 Å. An EELS detector semi-angle of 50 mrad and energy window of 40 eV above threshold was used. Line scans as a function of defocus for $x = 0$ Å are shown in (c) and (d) for probe apertures corresponding to (a) and (b), respectively. The total intensities are indicated by the solid lines, with signals due to the dopants at 62 and 130 Å indicated by the dotted and dashed lines, respectively.

inner-shell ionization necessary for EELS signals was shown to impose similar demands upon the detector collection semi-angle. Coupling experiment with rigorous theory is demonstrated to be paramount in avoiding erroneous image interpretation. The test cases explored only two scenarios of a vast number of relevant scenarios. This proof of concept study shows the viability of depth sectioning samples where HAADF is not capable of structure determination, namely imaging atoms lighter than the surrounding matrix.

Acknowledgements

L.J.A. acknowledges support by the Australian Research Council. This research was sponsored by the Office of Basic Energy Sciences, Division of Materials Sciences and Engineering, U.S. Department of Energy, under contract DE-AC05-00OR22725 with Oak Ridge National Laboratory, managed and operated by UT-Battelle, LLC and by appointment to the ORNL Postdoctoral Research Program administered jointly by ORNL and ORISE.

References

[1] M. Varela, A.R. Lupini, K. van Benthem, A.Y. Borisevich, M.F. Chisholm, N. Shibata, E. Abe, S.J. Pennycook, Annu. Rev. Mater. Res. 35 (2005) 539.
[2] P.A. Packan, Science 285 (1999) 2079.
[3] C.G. Van de Walle, Phys. Rev. Lett. 85 (2000) 1012.
[4] N. Shibata, S.J. Pennycook, T.R. Gosnell, G.S. Painter, W.A. Shelton, P.F. Becher, Nature 428 (2004) 730.
[5] S. Wang, A.Y. Borisevich, S.N. Rashkeev, M.V. Glazoff, K. Sohlberg, S.J. Pennycook, S.T. Pantelides, Nature Mater. 3 (2004) 143.
[6] A.Y. Borisevich, A.R. Lupini, S.J. Pennycook, Proc. Nat. Acad. Sci. 103 (2006) 3044.
[7] K. van Benthem, A.R. Lupini, M. Kim, H. Suck Baik, S.J. Doh, J. Lee, M.P. Oxley, S.D. Findlay, L.J. Allen, J.T. Luck, S.J. Pennycook, Appl. Phys. Lett. 87 (2005) 34104.
[8] J.J. Einspahr, P.M. Voyles, Ultramicroscopy 106 (2006) 1041.
[9] S.P. Frigo, Z.H. Levine, N.J. Zaluzec, Appl. Phys. Lett. 81 (2002) 2112.
[10] O.L. Krivanek, N. Dellby, A.R. Lupini, Ultramicroscopy 78 (1999) 1.
[11] P.E. Batson, N. Dellby, O.L. Krivanek, Nature 418 (2002) 617.
[12] P.M. Voyles, J.L. Grazul, D.A. Muller, Ultramicroscopy 96 (2003) 251.
[13] P.M. Voyles, D.A. Muller, E.J. Kirkland, Microsc. Microanal. 10 (2004) 219.
[14] A.Y. Borisevich, A.R. Lupini, S. Travaglini, S.J. Pennycook, J. Electron Microsc. 55 (2006) 7.
[15] R.F. Egerton, Electron Energy-loss Spectroscopy in the Electron Microscope, Plenum Press, New York, London, 1996.
[16] M. Born, E. Wolf, Principles of Optics, Cambridge University Press, Cambridge, 2003.
[17] O.L. Krivanek, P.D. Nellist, N. Dellby, M.F. Murfitt, Z. Szilagyi, Ultramicroscopy 96 (2003) 229.
[18] K. Ishizuka, J. Electron Microsc. 50 (2001) 291.
[19] L.J. Allen, S.D. Findlay, M.P. Oxley, C.J. Rossouw, Ultramicroscopy 96 (2003) 47.
[20] L.J. Allen, S.D. Findlay, M.P. Oxley, C. Witte, N.J. Zaluzec, Phys. Rev. B 73 (2006) 94104.
[21] S.D. Findlay, M.P. Oxley, L.J. Allen, Microsc. Microanal., 2006, submitted for publication.
[22] L.J. Allen, C.J. Rossouw, Phys. Rev. B 42 (1990) 11644.
[23] L.J. Allen, T.W. Josefsson, Phys. Rev. B 52 (1995) 3184.
[24] M.P. Oxley, L.J. Allen, Phys. Rev. B 57 (1998) 3273.
[25] P. Schattschneider, M. Nelhiebel, B. Jouffrey, Phys. Rev. B 59 (1999) 10959.
[26] P. Schattschneider, M. Nelhiebel, H. Souchay, B. Jouffrey, Micron 31 (2000) 333.
[27] N. Moret, D.Y. Oberli, E. Pelucchi, N. Gogneau, A. Rudra, E. Kapon, Appl. Phys. Lett. 88 (2006) 141917.
[28] S. Van Aert, A.J. den Dekker, D. Van Dyck, A. van den Bos, Ultramicroscopy 90 (2002) 273.
[29] E. Wolf, Proc. R. Soc. A 204 (1951) 542.
[30] C. Dwyer, Ultramicroscopy 104 (2005) 141.
[31] H. Kohl, H. Rose, Adv. Electron. Electron. Phys. 65 (1985) 173.
[32] E.C. Cosgriff, M.P. Oxley, L.J. Allen, S.J. Pennycook, Ultramicroscopy 102 (2005) 317.
[33] Y. Peng, P.D. Nellist, S.J. Pennycook, J. Electron Microsc. 53 (2004) 257.